

RESEARCH ARTICLE

Undulating fins produce off-axis thrust and flow structures

Izaak D. Neveln¹, Rahul Bale², Amneet Pal Singh Bhalla², Oscar M. Curet^{2,*}, Neelesh A. Patankar² and Malcolm A. MacIver^{1,2,3,‡}

ABSTRACT

While wake structures of many forms of swimming and flying are well characterized, the wake generated by a freely swimming undulating fin has not yet been analyzed. These elongated fins allow fish to achieve enhanced agility exemplified by the forward, backward and vertical swimming capabilities of knifefish, and also have potential applications in the design of more maneuverable underwater vehicles. We present the flow structure of an undulating robotic fin model using particle image velocimetry to measure fluid velocity fields in the wake. We supplement the experimental robotic work with high-fidelity computational fluid dynamics, simulating the hydrodynamics of both a virtual fish, whose fin kinematics and fin plus body morphology are measured from a freely swimming knifefish, and a virtual rendering of our robot. Our results indicate that a series of linked vortex tubes is shed off the long edge of the fin as the undulatory wave travels lengthwise along the fin. A jet at an oblique angle to the fin is associated with the successive vortex tubes, propelling the fish forward. The vortex structure bears similarity to the linked vortex ring structure trailing the oscillating caudal fin of a carangiform swimmer, though the vortex rings are distorted because of the undulatory kinematics of the elongated fin.

KEY WORDS: Fish locomotion, Undulating fin propulsion, Knifefish, Bio-mimetic, Bio-robotics, Digital particle image velocimetry (DPIV)

INTRODUCTION

A wide variety of fish undulate elongated fins to generate thrust. Knifefish undulate either an elongated dorsal fin, as is the case of the African knifefish *Gymnarchus niloticus*, or an anal fin, as is the case of species in the order Gymnotiformes and in the family Notopteridae. Triggerfish (family Balastidae) undulate both dorsal and ventral fins. Also, many species such as cuttlefish, skates and rays undulate elongated fins along their lateral margins. Undulatory motion, in contrast to oscillatory motion, implies that these fins produce a wave that travels along the fin with at least one full undulation present along the fin. These fish propel primarily by median and/or paired fin (MPF) propulsion, in contrast to body and/or caudal fin (BCF) propulsion where the fish propels by the actuation of the whole body, part of the body or only the caudal fin (for a review, see Sfakiotakis et al., 1999).

The biological model system used for this research is the elongated anal fin (hereafter termed the ribbon fin) of the weakly

electric knifefish, such as the fin present on the black ghost knifefish *Apteronotus albifrons* (Linnaeus 1766) (Fig. 1A). These knifefish are important model systems for studying sensory neurobiology (Turner et al., 1999; Krahe and Fortune, 2013) and sensory motor integration (Snyder et al., 2007; MacIver et al., 2010; Cowan and Fortune, 2007). Furthermore, research on the unique biomechanics and sensory modality of electric knifefish has inspired the design of numerous underwater robots capable of agile movement and omnidirectional close-range sensing (reviewed by Neveln et al., 2013).

Blake pioneered the research of ribbon fin propulsion in his study of knifefish (Blake, 1983), in which he described the kinematics of forward swimming fish. Subsequent work has quantified body kinematics (MacIver et al., 2001) as well as fin kinematics (Ruiz-Torres et al., 2013). Lighthill and Blake first modeled the hydrodynamics of the undulating ribbon fin using elongated-body theory (Lighthill and Blake, 1990). Work in our laboratory has examined the hydrodynamics of a non-translating undulating fin (Shirgaonkar et al., 2008), as well as measured the forces and free-swimming velocities generated by a biomimetic robotic ribbon fin, shown in Fig. 1B (Curet et al., 2011b). Results show that a single traveling wave along the fin is capable of producing both surge and heave components of thrust (see Fig. 1C for axes definitions). Knifefish can also partition their ribbon fin into two counter-propagating waves that originate on either end of the fin (Curet et al., 2011a; Ruiz-Torres et al., 2013; Sefati et al., 2013). Knifefish control the position of the point where the two waves meet along the fin to hover in still water and swim at slow speeds (Ruiz-Torres et al., 2013; Sefati et al., 2013). These counter-propagating waves on a single ribbon fin can be used to vary the proportion of surge and heave components of thrust (Curet et al., 2011a; Sefati et al., 2013).

Because of the unique properties of the propulsive mechanisms of the ribbon fin, weakly electric knifefish exhibit high maneuverability, including backward, upward and rolling motions. Even for time periods of the order of the sensorimotor neuronal delay time (~100 ms), they can maneuver to any location within their omnidirectional sensing range for small prey (Snyder et al., 2007). This tight coupling of sensory, neuronal and mechanical systems presents an interesting case study in the co-evolution of these complex, interdependent systems and the inherent trade-offs that occur when trying to maximize a relevant objective function such as the ratio of energy intake to expended energy (MacIver et al., 2010). A better understanding of the intricate mechanical properties of the ribbon fin is essential for further decoding the interdependency of sensory, neuronal and mechanical systems in this model system.

This study aims to further our understanding of hydrodynamic principles underlying cruising ribbon-fin swimmers through experimentation on a robotic model using digital particle image velocimetry (DPIV). We also use high-fidelity computational fluid dynamics of a virtual model of our robot and an accurate knifefish model with measured body and fin morphology combined with

¹Department of Biomedical Engineering, Northwestern University, Evanston, IL, USA. ²Department of Mechanical Engineering, Northwestern University, Evanston, IL, USA. ³Department of Neurobiology, Northwestern University, Evanston, IL, USA.

*Present address: Department of Ocean and Mechanical Engineering, Florida Atlantic University, Boca Raton, FL, USA.

‡Author for correspondence (maciver@northwestern.edu)

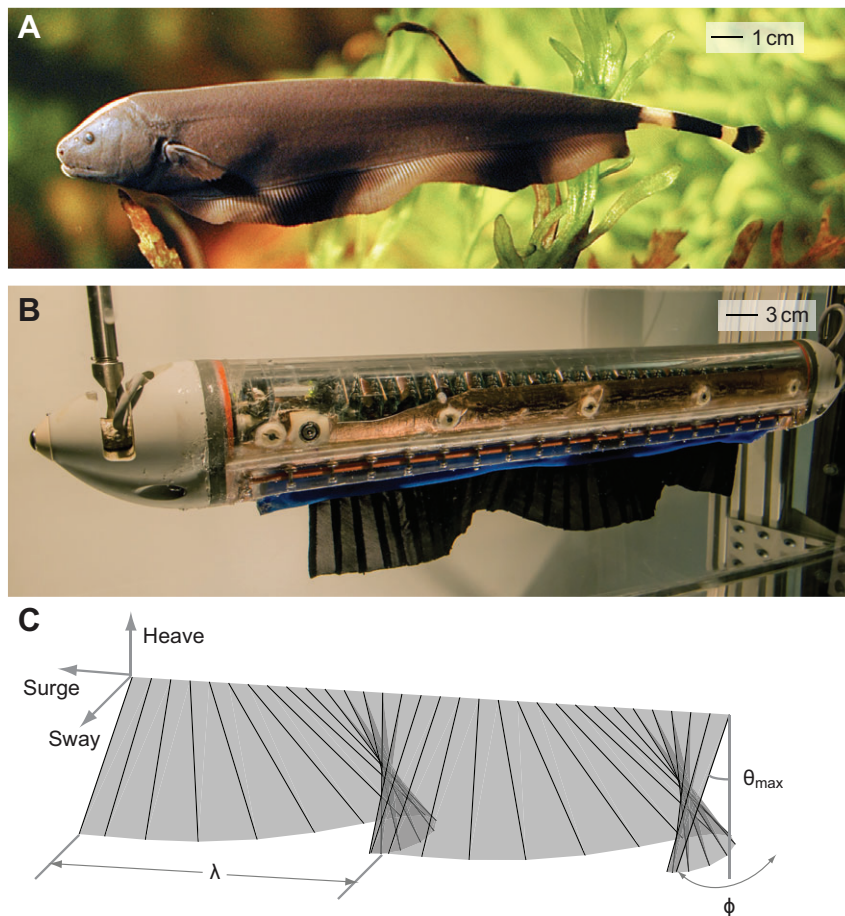


Fig. 1. The model system and its physical model. (A) The weakly electric black ghost knifefish, *Apteronotus albifrons*, a gymnotiform swimmer from the rivers of South America that undulates its elongated ventral fin, commonly termed the ribbon fin, to propel itself through fluid. Photograph courtesy of Per Erik Sviland. (B) The 'Ghostbot' swims using a biomimetic ribbon fin (black). The fin is 32 cm long and is actuated by 32 independent fin rays. (C) Schematic of the ribbon fin showing the wavelength (λ), angular fin amplitude (θ), ray oscillation frequency (ϕ), and the robot body frame (surge, heave and sway).

measured ribbon fin kinematics. We first describe the flow features present in the wake that are responsible for generating thrust along both the surge and heave axes of the fin. We then show the consistency of this flow structure across a range of ribbon fin sizes and kinematics with Reynolds numbers spanning over one order of magnitude. Finally, we introduce a schematic of the ribbon-fin wake vortex structure and compare MPF undulatory swimming to well-known BCF swimming mechanics under a framework for comparing flow structures using non-dimensional parameters such as wave efficiency and the Strouhal number.

RESULTS

Free-swimming velocities

The free-swimming pitched robot achieved a swimming speed of 26 cm s^{-1} ($0.8L_{\text{fin}} \text{ s}^{-1}$, where L_{fin} is fin length) for the kinematic parameters tested [frequency (f)=3 Hz, number of undulations=2, maximum angular amplitude (θ_{max})=30 deg]. Simulation FishSim1, which used the mean kinematic parameters of an actual free-swimming *A. albifrons* [14.9 cm s^{-1} data (from Ruiz-Torres et al., 2013)], obtained a steady-state swimming speed of 12 cm s^{-1} ($1.33L_{\text{fin}} \text{ s}^{-1}$). This speed underestimates the actual swimming speed of the fish by ~20%. Simulation FishSim2, which is the same morphology and kinematics as FishSim1 except that the amplitude envelope was constant at 30 deg, obtained a steady-state swimming speed of 17.7 cm s^{-1} ($1.97L_{\text{fin}} \text{ s}^{-1}$). The simulation of the robot, GhostbotSim, obtained a steady-state swimming speed of 26 cm s^{-1} ($0.80L_{\text{fin}} \text{ s}^{-1}$). The swimming speed matched the experimental robotic results very closely, providing validation of the simulation at the higher Reynolds number of the robot ($Re=80,000$) over that of the fish ($Re=13,000$). Finally, FinSim, which simulated an

undulating rectangular fin of the same length as the FishSim fins but without a body, swam 9 cm s^{-1} ($0.89L_{\text{fin}} \text{ s}^{-1}$). These results, as well as important kinematic parameters and non-dimensional numbers such as wave efficiency and Strouhal number, are reported in Table 1. More details about the simulations can be found in Materials and methods.

Wake patterns from DPIV planes

DPIV data were collected by imaging seven different planes of the swimming robot while submerged in a flow tunnel (Fig. 2). More details of the data collection and analysis can be found in Materials and methods.

Midsagittal plane

Fig. 3 shows both snapshots of the velocity vector field with corresponding vorticity as well as the average jet generated by the fin in the midsagittal plane M (Fig. 2B). In a particular time instant (Fig. 3A), velocity vectors (which have the incoming flow velocity subtracted) have varying directions along the length of the fin, alternating from more aligned in the surge direction to more aligned in the heave direction. A line of clockwise-rotating vortices are shed at an angle to the fin similar to the pitch angle of the fin (horizontal line of blue areas that intersects the front of the fin). Behind the fin, there are areas of vorticity with alternating sign. Fig. 3B shows the phase-averaged velocity vector field at the same instant in the cycle as Fig. 3A. Supplementary material Movie 1 shows the time evolution of the velocity vector field with associated vorticity over one cycle.

On average, the jet generated by the fin is aligned with the flow direction, as expected if thrust is aligned with swimming direction

Table 1. Fin parameters and free-swimming results

Parameter	FishSim1	FishSim2	GhostbotSim	Ghostbot	FinSim
Frequency, f (Hz)	10	10	3	3	3
Number of undulations, L_{fin}/λ	2.5	2.5	2	2	2
Maximum angular amplitude, θ_{max} (deg)	23	30	30	30	30
Specific amplitude, A/λ	0.22	0.28	0.31	0.31	0.20
Pitch angle (deg)	10	10	8	13	9
Free-swimming speed, U (cm s ⁻¹ , L_{fin} s ⁻¹)	12, 1.33	17, 1.93	26.5, 0.81	26, 0.80	9, 0.89
Wave efficiency, η	0.33	0.48	0.54	0.53	0.59
Strouhal number, St	0.65	0.58	0.57	0.58	0.34
Reynolds number, Re	13,000	13,000	80,000	80,000	8000

The dark gray cells highlight the fin parameters that were changed in the transition from FishSim1 to FishSim2. Note that the amplitude profile also change from a variable profile based off of actual fish data in FishSim1 to a constant profile in FishSim2. The light gray cells highlight the fin parameters that were changed in the transition from FishSim2 to GhostbotSim. Note also that the scale of the GhostbotSim was roughly three times the size of FishSim1 and FishSim2.

(Fig. 3C). This jet is strongest and deepest just downstream of the caudal end of the fin. The depth of the jet increases approximately linearly from the rostral edge of the fin to the caudal edge, and tapers off further downstream. There is a smaller secondary jet just downstream of the fin aligned along the surge axis of the fin.

Horizontal plane

Fig. 4 shows four snapshots of the phase-averaged velocity vector field and associated vorticity for the horizontal plane H (Fig. 2B). These snapshots split the fin cycle into quarters. Velocity vectors (which have the incoming flow subtracted) in the area of the plane transecting the fin are oriented largely laterally. Just downstream, vortices are shed off of the fin into the plane. These vortices alternate in rotational direction and are shed twice per fin cycle.

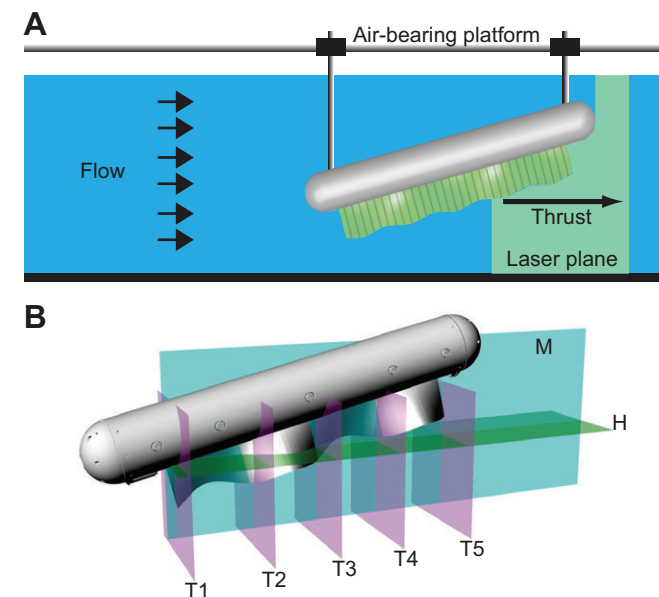


Fig. 2. Schematic of experimental setup. (A) The robot was suspended into a variable speed flow tank from a frictionless air-bearing platform. During digital particle image velocimetry (DPIV) experiments, the robot was fixed in place so that it would remain stationary in the laser plane, and the flow speed was set to match the previously determined free-swimming velocity for the robot with a pitch angle of 13 deg, frequency f of 3 Hz, wavelength λ of $L_{fin}/2$ and angular amplitude θ_{max} of 30 deg. (B) Data from seven DPIV planes were collected. The midsagittal plane (M) actually consists of three sets of DPIV data that were reassembled. The horizontal plane (H) consists of four sets of DPIV data, and intersects the fin edge approximately halfway along the length of the fin. Each of the transverse planes (T1–T5) consisted of a single set of data, and was approximately located at each quarter length of the fin length L_{fin} .

Fig. 4D outlines these vortices, where the area encompassed by a loop corresponds to the strength of the associated vortex. The velocity vectors associated with these vortices have both downstream and lateral components. Further downstream, the strength of the vorticity decreases, and the velocity vectors orient more along the direction of the flow. Supplementary material Movie 2 shows the time evolution of the velocity vector field with associated vorticity over one cycle.

Transverse planes

Fig. 5 shows four snapshots of the velocity vector field associated with the five transverse planes T1–T5. As in Fig. 4, the snapshots split the fin cycle into quarters. Because there are two undulations along the fin, the fin rays in T1, T3 and T5 are all roughly in phase with each other while in antiphase with the fin rays in T2 and T4. Supplementary material Movie 3 shows the time evolution of these planes over one cycle.

The velocity vectors in these transverse planes have the smallest magnitude in the anterior T1 plane, with magnitudes increasing moving posteriorly to T5. Vortices of alternating direction are present in each plane upon reversal of the fin ray, as indicated in Fig. 5D. These vortices are weakest in T1 and increase in magnitude moving posteriorly to T5. Consequently, the flow through these vortices is strongest in T5, while non-existent in T1. These flows are oriented mostly downward from the fin, with smaller lateral components that oscillate from left to right over a cycle. Also, vortices remain closely associated with the fin edge in T1 as the fin moves laterally, rather than being shed downwards off the fin edge as is evident in T5.

Simulation flow structure visualizations

To visualize the 3D wake structure of the simulations, we visualized iso-surfaces of the q -criterion (Dubief and Delcayre, 2000). The q -criterion subtracts the strain rate from the rotation rate of a velocity vector field, so that regions of positive q indicate vortical structures. Fig. 6 shows the bottom and side views of these iso- q surfaces for the four simulations. Vortical structures that are consistently present across the three simulations are indicated by the magenta arrows. These structures are vortex tubes that are initially shed by the rostral half-wave of the fin and then continually shed at the peaks of the waveform as the wave travels caudally. Supplementary material Movies 4–6 show the evolution of these structures over time. As the shed vortex tubes are left by the moving fin, they become entangled downstream to form a complex wake structure, until the strength of the vorticity dies out.

The fourth simulation, labeled FinSim, gives the clearest view of the wake structure. Supplementary material Movie 7 shows the

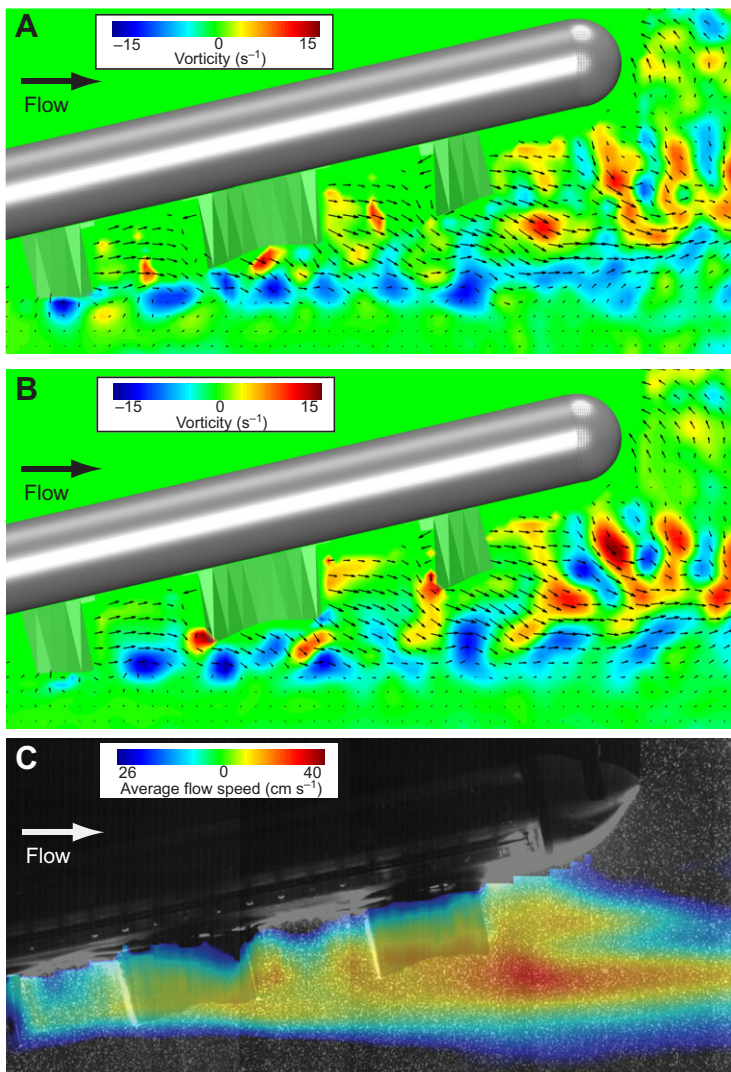


Fig. 3. Flow features in the midsagittal plane (plane M from Fig. 2B). (A) An instantaneous snapshot of the velocity vector field in the midsagittal plane with the mean swimming velocity ($U=26\text{ cm s}^{-1}$) subtracted. The colormap indicates the vorticity. A line of clockwise vortices emanate from near the front of the fin at an angle to the fin close to the pitch angle of the robot (blue areas along horizontal line that intersects the front of the fin). See supplementary material Movie 1 for the corresponding video. (B) The phase-averaged velocity vector field and corresponding vorticity at the same time in the cycle as A. (C) The average jet generated by the traveling wave of the fin. The colormap indicates the magnitude of the fluid velocity field averaged over many cycles. The jet is aligned with the swimming direction, and is strongest immediately downstream of the fin.

evolution of the iso- q surfaces, and a snapshot view is included in Fig. 6D for comparison with the other simulations. The flow structures in FinSim are less entangled than those in FishSim1 and FishSim2, likely because the traveling wave frequency is less by more than a factor of three (Table 1), giving a clearer view of the wake. However, the manner in which these vortex tubes are shed is similar to the shedding of vortex tubes from the other simulations.

DISCUSSION

Both the experimental and computational results indicate that the wake structure across both fish and robot body and fin morphologies maintain the same qualitative features. First, we discuss how exactly the flow features of the 2D DPIV planes map to the overall 3D vortical structure of the wake. Second, we compare the 3D wake of free-swimming ribbon fins with prior results from a non-translating undulating fin (Shirgaonkar et al., 2008). Third, we introduce important relationships between the kinematic parameters of the undulating fin and non-dimensional numbers associated with free swimming such as wave efficiency (sometimes referred to as slip) and Strouhal number. Fourth, we relate these non-dimensional numbers to the wake structure of the undulating ribbon fin. Last, we compare the wake of the ribbon fin with the well-characterized wake of carangiform swimming, showing specifically how knifefish have

maintained similar thrust-producing mechanisms with a fin of drastically different morphology and kinematics.

3D schematic of vortex tubes shed from the fin edge

There has been some effort to show how experimental 2D DPIV data correlate with hypothesized 3D wake structures in various forms of swimming. For example, the wake of a carangiform swimmer with an oscillating caudal tail is thought to generate a series of connected vortex rings (Nauen and Lauder, 2002). A horizontal slice through these vortex rings illuminates the classic reverse von Kármán vortex street visible in planar DPIV measurements (Nauen and Lauder, 2002). Similar reverse von Kármán vortex streets are present in the transverse planes measured for the Ghostbot fin, especially in T3–T5 (Fig. 5). The vortices in the transverse planes must be sections of a 3D vortex structure. Indeed, a vortex tube is shed as the wave travels along the length of the fin, as seen in the iso- q surfaces of the simulations (Fig. 6, supplementary material Movies 4–7).

The vortex tubes shed from the fin edge also account for the other vortices present in the horizontal and midsagittal planes. In the horizontal plane, strong vortices are present at the posterior point of the intersection between the fin and the plane, indicated by the solid white line in Fig. 4. These vortices are lengthwise slices through the vortex tube as it is being shed, orthogonal to the slices in the

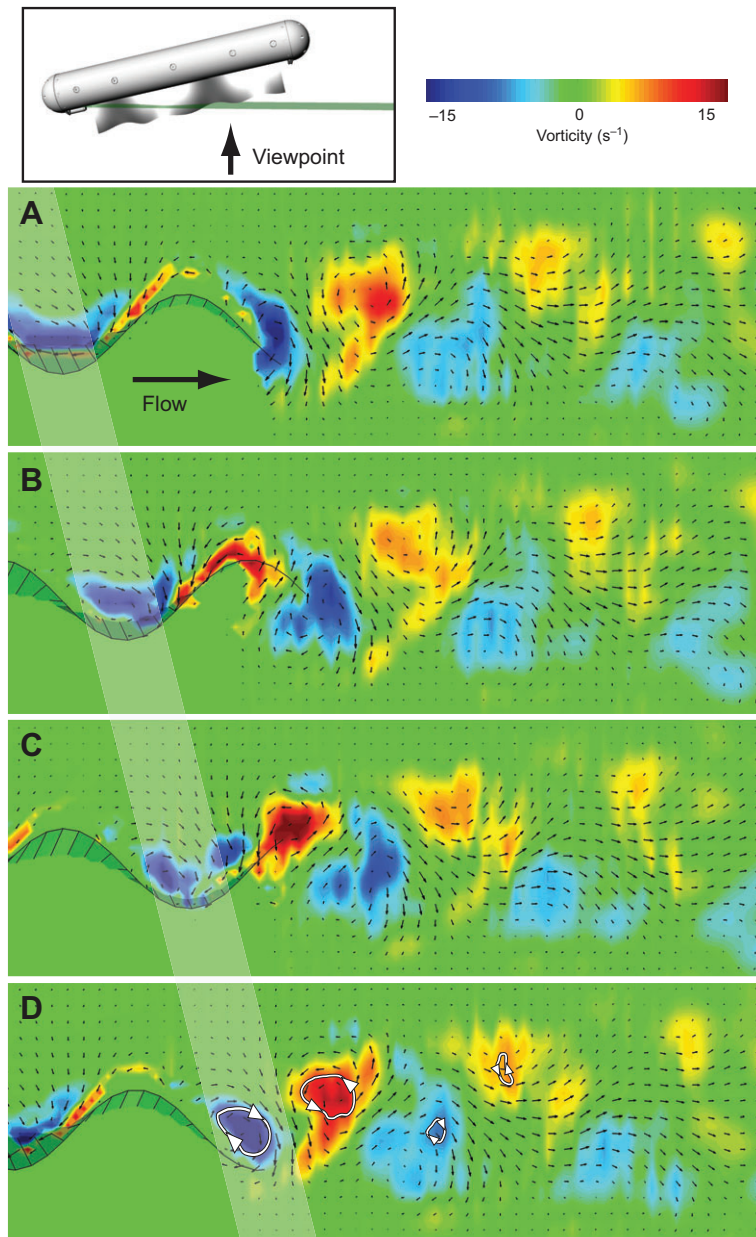


Fig. 4. Flow features in the horizontal plane (plane H from Fig. 2B). Velocity vector fields were measured in a plane horizontal with respect to the wake structure (see inset for plane position and viewpoint). The vertical position of this plane was selected to bisect the wake. (A–D) Four phase-averaged snapshots within one cycle at $t=0.25T$ (A), $t=0.50T$ (B), $t=0.75T$ (C) and $t=T$ (D), where t is instantaneous time and T is one period. The vortices are outlined with white arrows in D to show the sense of rotation as well as relative magnitude of the vorticity, which is indicated by the size of the closed loops. The movement of the traveling wave is indicated by the transparent white strip. See supplementary material Movie 2 for the corresponding video.

transverse planes. In the midsagittal plane, a series of similarly rotating vortices are shed in a line at an angle to the fin closely matching the pitch angle of the robot (Fig. 3). Again, 2D vortices are slices through the vortex tubes shed off the fin. As seen in Fig. 6, the vortex tubes bend medially towards the opposing side and cross the midsagittal plane. Successive vortex tubes have opposite rotation in the transverse plane (Fig. 5), but are also shed on opposite sides of the fin. Therefore, when the vortex tubes bend medially and intersect the midsagittal plane, every vortex tube has the same rotational direction such that higher downstream flow (indicated by the light blue color) is closer to the fin. Over the course of a cycle, this high downstream flow averages to the jet visible in Fig. 3C.

The shedding and distortion of the fin edge vortex tubes are schematized in Fig. 7. Vortex tubes are color-coded based on the side of the fin from which they are shed. This schematic encapsulates many of the main features present in the vortex tubes shed by the fin edge. Towards the rostral portion of the fin, where the tube is just starting to be shed, the tube is oriented laterally due to being shed at

a single time by the rostral half wave of the fin (Fig. 7A). Each vortex tube should be connected to the previous tube as well as the subsequent tube according to Helmholtz's second theorem of vorticity (Kuethe and Schetzer, 1950). The schematic details this connection for the anterior part of these tubes, though they should also connect on the posterior ends of the tubes after being shed off the back of the fin. In between, the vortex tube remains roughly in the location where that portion of the tube was shed (Fig. 7B). Therefore, the downstream spacing of subsequent vortex tubes is mostly determined by the swimming speed of the fin. We will return to the issue of vortex spacing in further discussion below.

The wake structure remains consistent throughout all simulations, which range in Reynolds number over approximately one order of magnitude. Fig. 6 highlights the consistent vortex structures when viewed from below. Furthermore, Fig. 8 compares the midsagittal plane of the schematics with the DPIV data as well as all four simulations. In Fig. 8B–E, the line of blue vortices emanating from the fin along the direction of swimming is consistent with the lateral

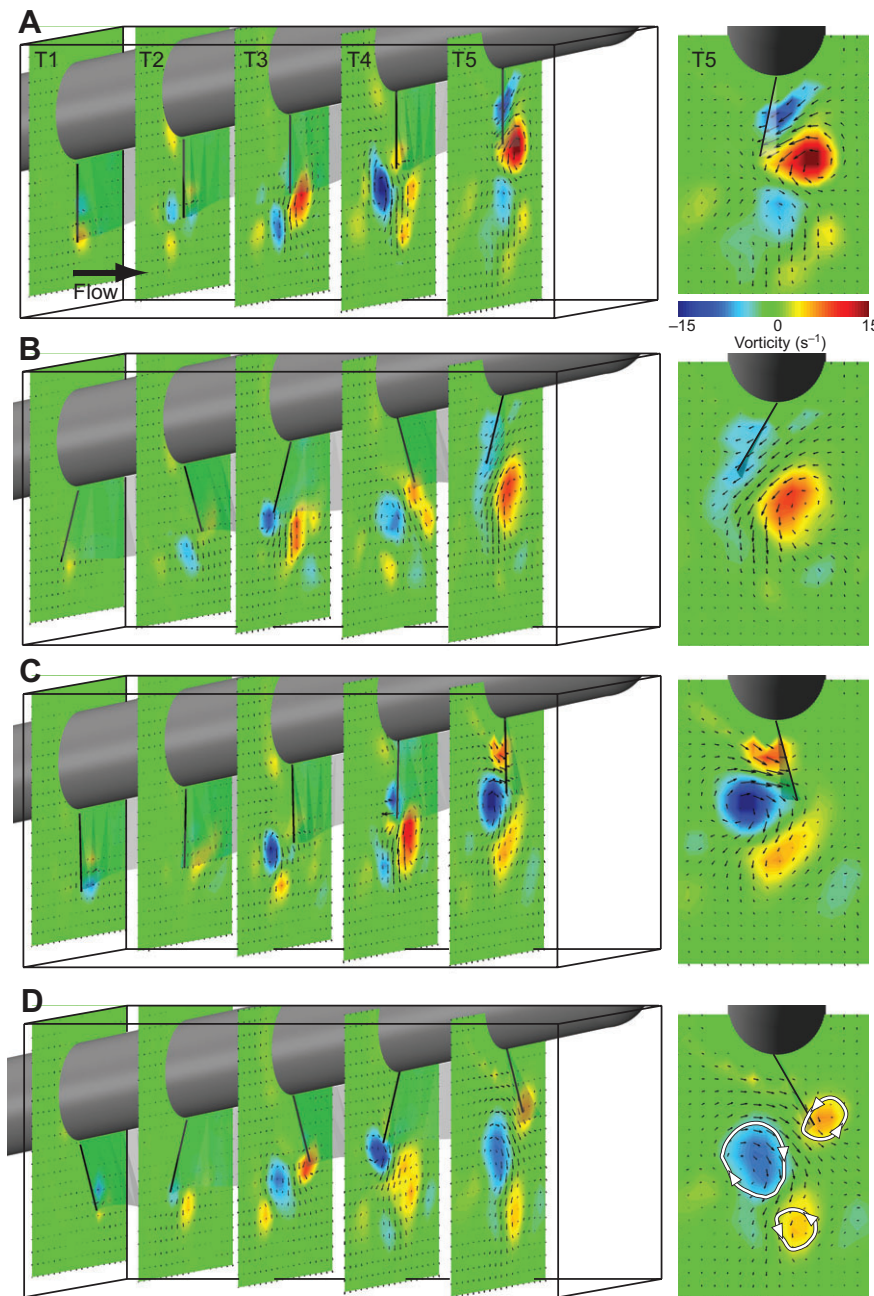


Fig. 5. Flow features in the transverse planes (planes T1–T5 from Fig. 2B). Phase-averaged velocity vector fields for the five transverse planes are shown as they correspond to actual fin motion. (A–D) Four snapshots within one cycle, as in Fig. 4. Plane T5 at the downstream edge of the fin indicates that counter-rotating vortices are shed each time the fin changes its lateral direction. There is an associated jet of fluid through these vortices with a strong downward component of the fin edge. This flow pattern weakens for the more upstream planes, to the point where in plane T1 the vortices are not shed and there is little downward flow off the fin edge. A normal view of plane T5 is included to give a clear picture of the reverse von Kármán vortex street, which is specifically outlined in plane T5 of D. See supplementary material Movie 3 for the corresponding video.

reorientation of the edge vortex tubes. Fig. 8E further shows the connection between the vorticity in the midsagittal plane and the 3D vortex structure. Whether robot scale, fish scale or without any body, the wake structure remains qualitatively similar.

Comparison of wake structures from free-swimming and non-translating ribbon fins

The hydrodynamics of elongated ribbon fin propulsion is highly complex with significant 3D effects. Previously, we investigated the hydrodynamics of a non-translating undulating ribbon fin in stationary water (Shirgaonkar et al., 2008). This flow condition was used to explore the hydrodynamics of impulsive motion. Impulsive motion is common in knife-fish as they are constantly changing their direction of motion during prey capture (MacIver et al., 2001).

The non-translating undulating fin produced both surge and heave forces, just as the average velocity of a freely swimming fin has both

surge and heave components. We attributed the heave forces in the non-translating case to vortex tubes generated by the fin edge as it oscillates back and forth laterally. Similarly, Fig. 5 shows how the vorticity generated and shed by the fin edge creates a flow with large heave components. We attributed the surge forces in the non-translating case to the longitudinal jet created by the motion of the traveling wave. We inferred that the primary vortex rings encircling the jet were induced by the flow and were separate from the vortex tubes generated by the fin edge. However, in the current free-swimming simulations as well as the DPIV data, we see that the vortex tubes shed by the fin become distorted and actually wrap around the overall jet shown in Fig. 3. Consequently, the vortex rings and the fin edge vortex tubes that were previously thought to be separate phenomena associated with surge and heave forces, respectively, are likely different parts of the same vortex structures shed by the fin. A comparison of these vortex rings of the current

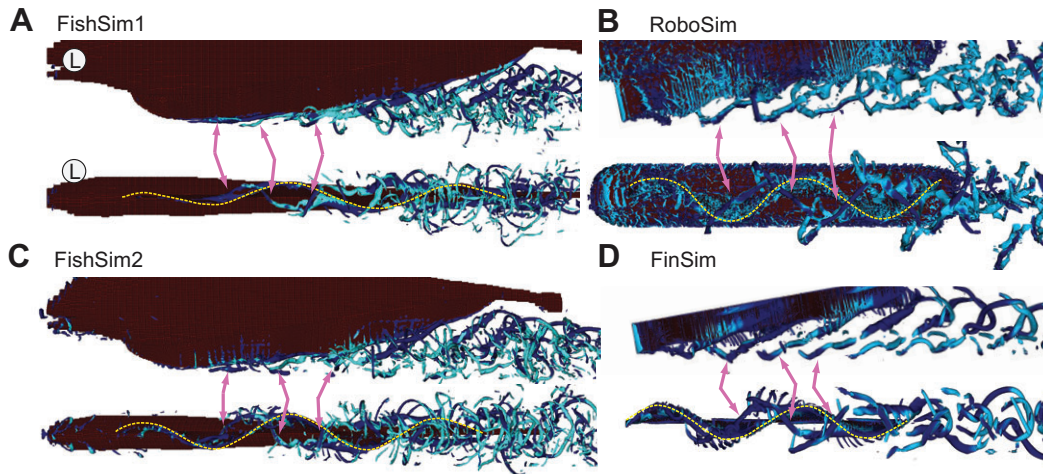


Fig. 6. 3D flow structure comparison. Bottom and side views of the 3D flow structure is shown for the four simulations: FishSim1 (A), RoboSim (B), FishSim2 (C) and FinSim (D). The structures are an iso-surface of the q -criterion (called iso- q surfaces) and are colored such that dark blue indicates upstream flow velocities and light blue indicates downstream flow velocities. The fin edge is outlined with a dashed yellow line for the bottom views. Vortex tubes are indicated by the pink arrows at the points where they cross laterally over the midsagittal plane. These vortex tubes share many qualitative similarities across all four simulations, including how they are shed from the fin edge as well as how they bend laterally to connect to one another. The 'L' in A indicates the anatomical left side of the fish for both the side and bottom views, which remains consistent throughout B–D.

FinSim and the non-translating fin from Shirgaonkar et al. (Shirgaonkar et al., 2008) is shown in Fig. 9.

Relationship between Strouhal number, wave efficiency and fin parameters

For any undulatory swimmer in which a traveling wave is present, a wave efficiency η can be defined as:

$$\eta = \frac{U}{V_{\text{wave}}}, \quad (1)$$

where U is the free-swimming speed and V_{wave} ($=f\lambda$) is the speed of the traveling wave. η has a range of 0–1, where 0 indicates no longitudinal movement and 1 indicates that the fin is moving forward as fast as the traveling wave moves backward. η therefore is labeled as a measure of efficiency, as for the best-case scenario where $\eta=1$, the fish achieves the highest output velocity for the velocity given to the traveling wave. In our simulations and robotic experiment, the wave efficiency ranges from 0.3 to 0.55 (Table 1), whereas *A. albifrons* has been recorded to achieve wave efficiencies as high as 0.7 (Ruiz-Torres et al., 2013).

The Strouhal number (St) has been cited as an important non-dimensional number for unsteady, periodic flows such as those found in the wake of fishes (Triantafyllou et al., 1991; Lauder and Tytell, 2006). The equation for St is:

$$St = \frac{fA}{U}, \quad (2)$$

where f is the frequency of ray oscillation and A is a length associated with the oscillation (defined in this work as the peak-to-peak lateral excursion of the fin). The range of St for cruising swimmers and fliers of various sizes is between 0.2 and 0.4 (Taylor et al., 2003). The simulations and free-swimming robotic data presented here exhibit St between 0.3 and 0.65 (Table 1).

St can be considered to indicate the ratio of local inertial forces to convective inertial forces, or in the case of a swimming fish, the ratio of local momentum input to the wake by the fin to the output momentum imparted on the fish by the wake, which moves the fish forward. Therefore, St can be considered a second measure of

efficiency, where the fin aims to achieve the highest swimming velocity while minimizing lateral fin velocity. When St is considered as a type of efficiency, clearly a lower St implies better performance, with $St=0$ indicating perfect performance. The natural range of 0.2 to 0.4 for St indicates that there exists a practical lower limit of around 0.2 (gliding is a case where $St=0$, though the gliding velocity is not constant over time).

As η and St are indirect indicators of efficiency, how do these two parameters depend on each other? Multiplying Eqn 1 (with $f\lambda$ substituted for V_{wave}) by Eqn 2 results in:

$$\eta St = \frac{A}{\lambda}, \quad (3)$$

where the quantity A/λ is termed the specific amplitude (in this case the peak-to-peak amplitude). This relationship implies that for a given specific amplitude, there is a lower limit for St for the maximum value of $\eta=1$. Therefore, to decrease the lower limit of St , the specific amplitude of the traveling wave must be diminished, either by decreasing A or increasing λ . However, assuming there is a physical lower limit to St of 0.2, decreasing the specific amplitude also decreases the maximum achievable η . For example, if the highest achievable η was 0.5 and the lowest achievable St was 0.2, the specific amplitude would necessarily be 0.1.

It should be noted that a better measure of efficiency for a cruising animal or robot would relate the total input power (P) to the system to the useful output power, such as propulsive efficiency ($\eta_p = FU/P$, where F is thrust or drag) or cost of transport ($COT = P/U$). For example, Anderson et al. found that η_p was maximal for St in the range of 0.25 to 0.40 for an oscillating foil with varying kinematics (Anderson et al., 1998). Moreover, Moored et al. found a local maximum of η_p when the driving frequency of an oscillating fin matched the hydrodynamic resonant frequency (Moored et al., 2012). However, these oscillating foils were not self-propelled. While we did not measure input power to the system, we would expect the power needed to drive the rays of either the robot or the fish to increase with ray velocity, which increases with both frequency and amplitude of oscillation, parameters in the numerator of St . Therefore, we expect COT to follow similar trends as St , and

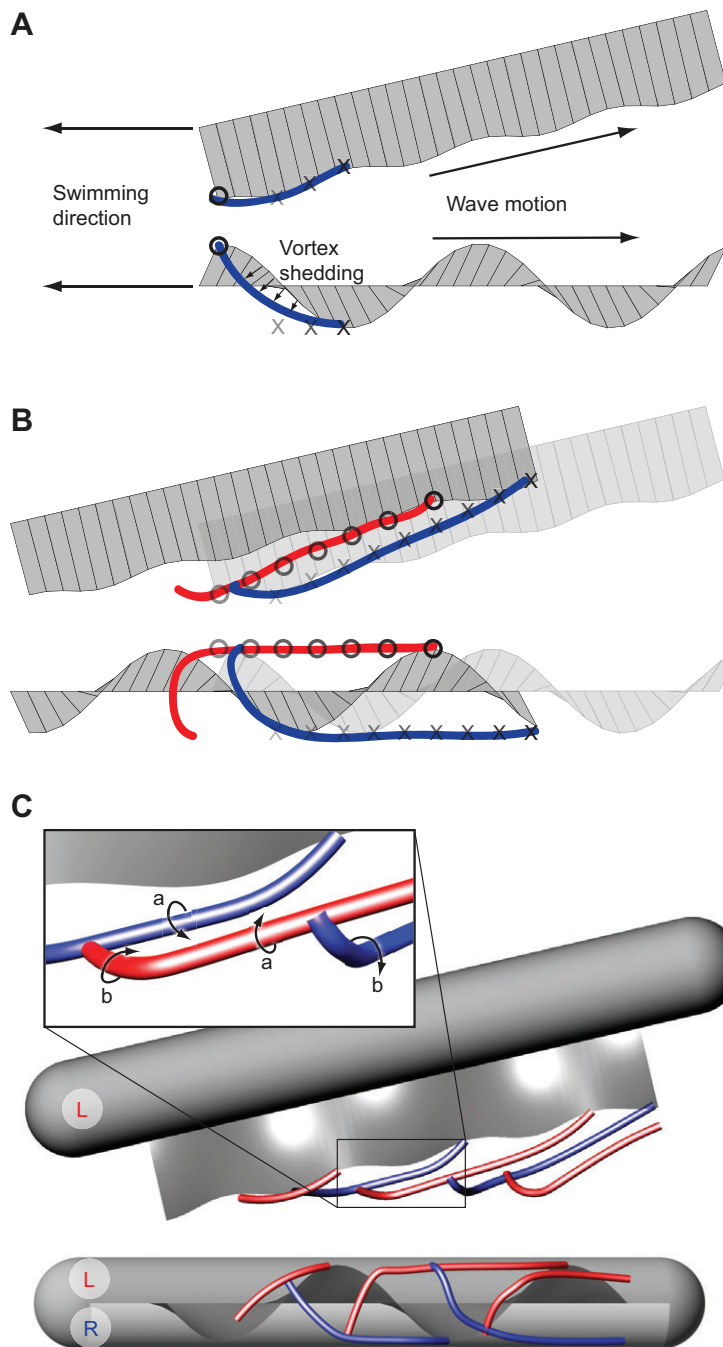


Fig. 7. Schematic of 3D vortex structure. (A) Vortex tube as it begins to shed from the fin. In this schematic, locations of the waveform peaks over time are indicated with Xs and Os, where the solid black symbols indicate the present location of the peaks while faded symbols indicate previous locations. The vortex tube associated with the Xs just begins to shed as the subsequent waveform peak represented by the Os appears on the fin. (B) The later position of the fin after the waveform peak represented by the Xs reaches the back of the fin. The original position of the fin from A is included as a faded silhouette. The blue vortex tube associated with the X peak joins with the subsequent vortex tube associated with the O peak in approximately the same location as the fin in A. Otherwise, the vortex tubes follow the locations where the peaks of the waveform transversed. Only two vortex tubes and corresponding peaks are shown for clarity. (C) Snapshot of multiple successive vortex tubes. Each vortex tube is shed as the corresponding peak of the waveform travels from the front to the back of the fin. The vortex tubes have been colored to indicate whether they were shed from the left (red) or right (blue) side of the fin. Each vortex tube is directed laterally to join with the following tube as in B. Similar linking is expected further downstream in the wake as the tubes are shed off the rear of the fin. The expanded view of the vortex tubes shows the sense of rotation with circular arrows. The two arrows marked 'a' indicate opposite directions of rotation of the red and blue tubes in the orthogonal transverse plane away from the midsagittal plane, while the two arrows marked 'b' indicate the same direction of counter-clockwise rotation of two tubes as they cross the midsagittal plane. These midsagittal vortex tube sections correspond to the horizontal line of blue vortices from the 2D DPIV data from Fig. 3A.

that the lowest St values observed are approaching the best propulsive efficiencies achievable.

Wake structure in terms of St and η

More pertinent to the focus of this study is the relationship of St and η to the actual wake structure generated by the fin. In these free-swimming cases, the vortex tubes shed off the fin exhibit a small downstream velocity component relative to the surrounding fluid. Therefore, the spacing of adjacent vortex tubes in the direction of swimming is mostly determined by the swimming speed, U . Because two vortex tubes are shed for every ray cycle, the vortex spacing S along the direction of motion is approximately:

$$S = \frac{U}{2f}. \quad (4)$$

Substituting Eqn 4 into Eqn 1 and solving for S gives:

$$S = \frac{\eta\lambda}{2}, \quad (5)$$

and similarly, substituting Eqn 4 into Eqn 2 and solving for S gives:

$$S = \frac{A}{2St}. \quad (6)$$

From both of these relationships, it is clear that higher wave efficiencies and lower Strouhal numbers result in larger vortex spacing. Higher vortex spacing indicates that the fin is obtaining more impulse per vortex tube, which would indicate greater efficiency. It is hypothesized from the well-studied carangiform wake, however, that a vortex spacing resulting in a reverse von Kármán street with associated linked small core vortex rings is the

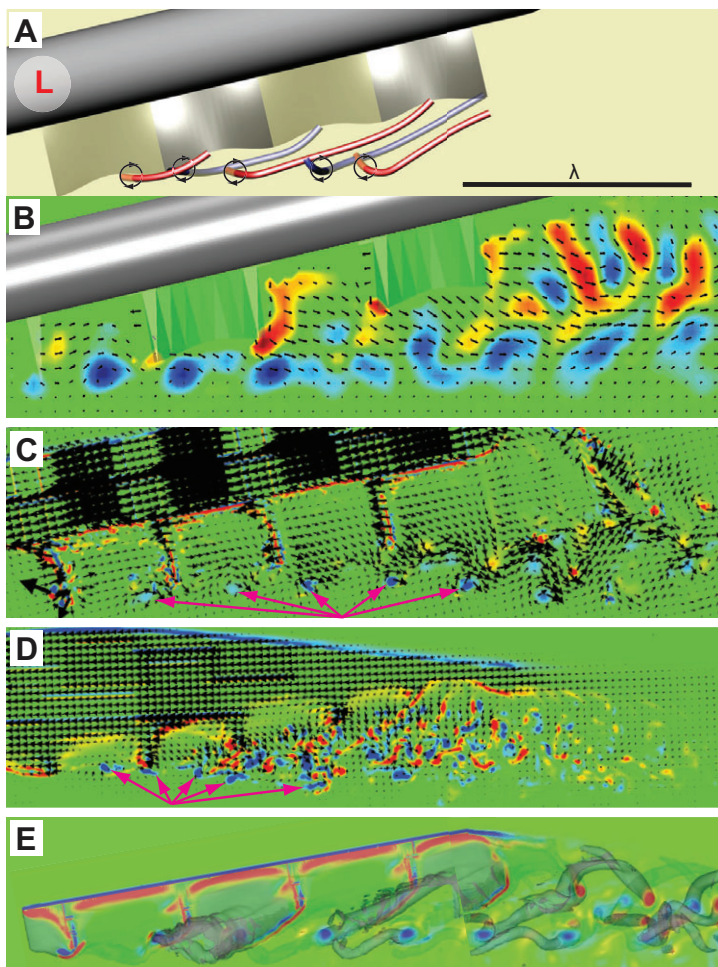


Fig. 8. Comparison of wake structure in the midsagittal plane. (A) Midsagittal view of schematic. The schematic from Fig. 7C with a transparent gray midsagittal plane shows where each vortex tube crosses the plane. Consecutive vortex tubes are shed from opposite sides of the fin, as indicated by the color of the tubes. Each vortex tube has the same sense of vorticity when crossing through the midsagittal plane as described in Fig. 7C. The scale bar shows the wavelength, where each image in A–E has been scaled so that wavelength is consistently sized. (B) Midsagittal view of DPIV data. The midsagittal plane from Fig. 2B is shown again for comparison. The line of blue vortices corresponds with the traversals of the shed vortex tubes across the midsagittal plane. (C) Midsagittal view of RoboSim. This view shows a line of vortices similar to that shown in B, marked by magenta arrows for clarity. (D) Midsagittal view of FishSim1. The line of vortices, indicated by the magenta arrows for clarity, is still present, though the vortices are spaced more closely together. The spacing of the vortices is dependent on wavelength and wave efficiency (Eqn 5). As wavelength is scaled the same across each case, a closer spacing indicates a smaller wave efficiency, which is the case for FishSim1 (see Table 1). (E) Midsagittal view of FinSim. The vorticity for the midsagittal plane of FinSim is shown with the 3D iso-vorticity structure (transparent) to show the correlation between the planar vorticity and the overall wake structure. In this case, the vortices are spaced further apart as the wave efficiency is highest.

signature of highly propulsive thrust (Nauen and Lauder, 2002). These linked rings seem to limit the vortex spacing, which in turn limits St . For example, when $St=0.2$, $S=2.5A$, so for vortex spacing greater than this value the linked vortex pattern likely becomes unlinked and breaks down. Further discussion on predicting St from measured distances associated with the wake for ribbon fins as well as other forms of swimming is provided in a later section.

There have been a few studies relating the wake structures to St in both anguilliform and carangiform forms of swimming. A series of articles by Borazjani and Sotiropoulos show in simulation that as Reynolds number increases, St decreases for free-swimming carangiform and anguilliform swimming (Borazjani and Sotiropoulos, 2008; Borazjani and Sotiropoulos, 2009). For low Reynolds numbers ($Re=300$ and 4000), St was always around 0.6 or above. The St fell within the observed range of 0.2 to 0.4 only for the inviscid simulations. For these low St scenarios, the wake was a single row wake structure consistent with the linked vortex rings associated with carangiform swimming. For higher St , the wake split into a double row wake structure. In self-propelled cases, the transition from single row to double row wake structure seems to occur as the vortex spacing decreases past a critical value, corresponding with increasing St . We expect that if the ribbon fin swam at higher St , a similar double row wake structure would develop. Other studies of heaving and pitching foils in an imposed flow show that changes in the effective angle of attack also can cause the transition from single row to double row wake structure (Blondeaux et al., 2005; Dewey et al., 2012).

For undulatory fins such as the knifefish fin, the vortex spacing also depends on wavelength and wave efficiency given by Eqn 5. This

trend is visible in Fig. 8, where the spacing of the line of vortices in the midsagittal plane is determined by the wave efficiency, as the wavelength is scaled in each image to be equal. For a case with high wave efficiency, such as FinSim (Fig. 8E), the spacing is visibly larger than a case with low wave efficiency, such as FishSim1 (Fig. 8D). Clearly, if wavelength were further decreased, the vortex spacing would decrease, resulting in interference between adjacent vortex tubes. However, if wavelength was increased, the surge component of the thrust would vanish, as described in the following section.

Connecting the wake of the ribbon fin to that of carangiform swimming

The feature of the ribbon fin that differentiates it from most other forms of underwater propulsion is that the thrust produced has components in both the surge and heave axes. For that reason, there exists a consistent insertion angle of the fin to the body, so that the longitudinal axis of the body aligns more with the direction of thrust and the corresponding wake. The ribbon fin can even vary the proportion of the surge component of thrust to the heave component of thrust, though fish accomplish this mainly using two counter-propagating waves (Curet et al., 2011a; Sefati et al., 2013). Can the flow structure for a single traveling wave be broken into heave features and surge features? Consider the wake generated by an oscillating caudal fin of a carangiform swimmer such as a trout, as shown in Fig. 10A. As mentioned, the wake consists of a series of linked vortex rings, with an increased flow through those rings. There are two vortex rings per cycle, and each associated jet has a lateral component with alternating direction. The height of the ring

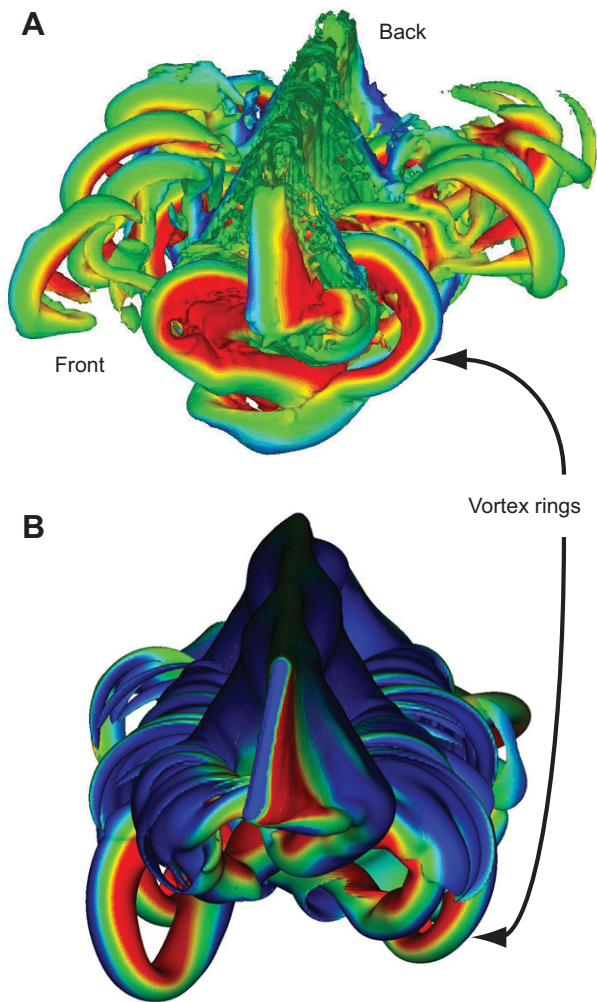


Fig. 9. Comparison between free-swimming and non-translating ribbon fins. (A) Front view of the vortex structure from a non-translating fin (Shirgaonkar et al., 2008). In this previous study, we investigated the hydrodynamics of impulsive motion through simulations of a non-translating undulating fin. Vortex rings surrounded the jet created by the traveling wave along the fin. The iso-vorticity surface was colored by the axial flow velocity, where red indicates downstream flow velocities and blue indicates upstream flow velocities. Therefore, the red interior of these rings indicate a propulsive jet. (B) Front view of the vortex structure of the freely swimming FinSim. Vortex rings similar to those in A wrap around the fin, here visualized with iso-vorticity surfaces and colored similarly to A. These vortex rings clearly originate from the fin edge, and are distorted to circle the fin, leading us to conclude that the vortex rings from the previous non-translating simulations originate from the fin edge as well. The main difference between the two cases is that the vortex rings in the non-translating case become more closely spaced as the fin is not able to move away from the regions where the rings are shed.

is on the order of the height of the fin, while the axial spacing of the rings is determined mostly by the Strouhal number and the amplitude of oscillation.

The structures created by a trout surging can be related to the structures generated by a ribbon fin if it were to be actuated with a traveling wave of infinite wavelength. In this case, as shown in Fig. 10B, each ray of the fin is in phase with every other ray, so the fin oscillates similarly to the caudal fin of a trout. This oscillation is now centered around the heave axis of the ribbon fin instead of the surge axis of the caudal fin, and would tend to move the fish in the fin-fixed heave direction. Assuming an appreciable velocity could be reached so that St fell within the range of ~ 0.2 to 0.4 , we predict

that the wake would contain a similar trail of linked vortex rings, now with the width of the rings on the order of the length of the fin as shown in Fig. 10B.

Moving to the biological case of an undulating fin with a finite wavelength, as shown in Fig. 10C, the portions of the vortex tubes that bend up from the rostrocaudally stretched tube are no longer shed simultaneously, but over a period of time as the wave travels along the fin. This wave motion in the surge direction contributes momentum to the fluid along that axis so that a surge component of thrust emerges. The vortex rings are now realigned along a line at an angle ventral to the fin, approximately the same angle as the insertion angle of the fin to the body. The eel-like undulatory motion of the ribbon fin is responsible for this realignment of the wake structures and therefore the off-axis direction of thrust. However, the vortex ring pattern has more in common with the small core linked vortex rings found in the wake of carangiform swimmers than with the double row wake structures found in anguilliform locomotion (Tytell and Lauder, 2004; Kern and Koumoutsakos, 2006).

The predictive power of a ribbon fin ‘footprint’

The wake of a fish can be considered the ‘footprint’ of the fish. We have described the footprint of an undulating fin and explored the similarities and differences compared with the footprints of other forms of underwater locomotion. The larger structure of the wake of a self-propelled fish can predict the swimming mode. First, a wake with double row vortex rings and associated lateral jets implies an anguilliform swimmer (Tytell and Lauder, 2004; Kern and Koumoutsakos, 2006). Second, a wake with a single row of linked vortex rings and associated downstream jet implies a carangiform swimmer (Nauen and Lauder, 2002). Third, a wake with a single row of diagonally distorted and linked vortex tubes implies an undulating ribbon fin swimmer. It is important to note that the transition from a single row wake to a bifurcated double row wake is due mostly to the differences in St exhibited by anguilliform and carangiform swimmers, and not simply to differences in kinematics (Tytell et al., 2010), leading us to predict that if a ribbon fin fish swam at a higher St , the wake would begin to bifurcate.

Furthermore, a closer examination of the vortex structure can produce an estimation of St . Using the equation for the vortex spacing along the swimming direction in terms of St (Eqn 6), we can predict St by measuring the distance between successive vortex tubes or rings as well as the width of the wake (which corresponds to A in Eqn 6). The lower the ratio of the wake width to the vortex spacing, the lower the St , indicating a fish that is able to swim further per ‘footprint’. These predictions can be extended to the bifurcating wake of an eel, where the distance S is the streamwise distance between two alternating vortex rings, which is indeed much smaller than that of a carangiform swimmer, hence the difference in St .

MATERIALS AND METHODS

The robotic knifefish

To study the flow structures of ribbon fin propulsion, we used a mechanical fin model that mimicked the undulatory kinematics of the ribbon fin. The mechanical fin was a slightly modified version of the knifefish-inspired ‘Ghostbot’ (Fig. 1B) used in a number of previous studies (Curet et al., 2011a; Curet et al., 2011b; Sefati et al., 2013). The fin remained 32.60 cm long (L_{fin}), but was modified to be 5.00 cm deep (h_{fin}), rather than the 3.37 cm in prior studies, to generate a higher amount of thrust. The Ghostbot is roughly three times the length of an adult black ghost knifefish like the one shown in Fig. 1A. The fin was actuated by 32 stainless steel rays, emulating the bony rays of the knifefish ribbon fin, each driven independently by a servo motor (Curet et al., 2011b). The fin membrane connecting these rays was lycra fabric, which had an elastic modulus of ≈ 0.2 MPa, similar to the collagenous

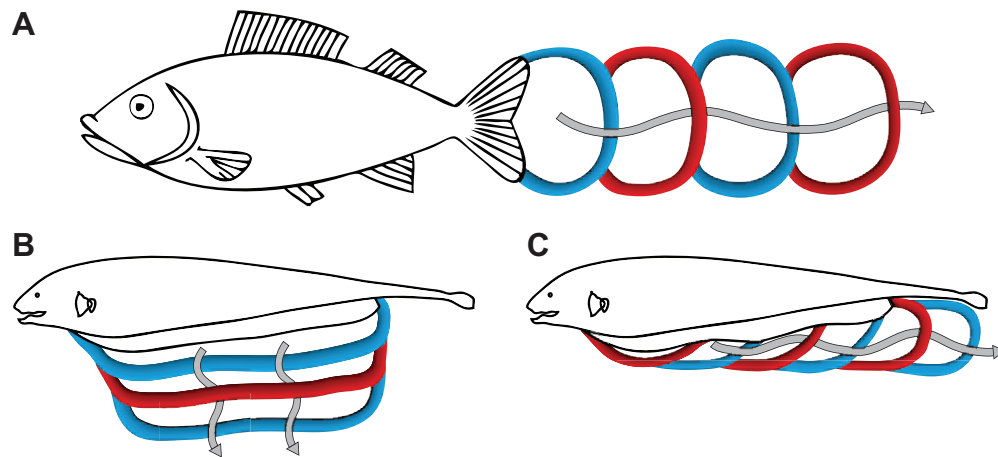


Fig. 10. Comparison of wake structures across swimming modes. (A) A carangiform swimmer such as a trout creates a wake consisting of linked vortex rings when cruising. (B) In the hypothetical scenario in which the ribbon fin of a knife-fish oscillates with no traveling wave, the wake structure might bear similarities to the carangiform wake if the knife-fish could swim in the heave direction at similar Strouhal numbers (St). The vortex rings become elongated, matching the elongation of the anal fin. (C) As the ribbon fin transitions from purely oscillatory to undulatory kinematics with a wavelength smaller than the fin length, the vortex rings become reoriented because of the motion in the surge direction, matching the vortex structure from the 3D schematic in Fig. 7. If the amplitude of the fin motion was the same for both the carangiform swimmer in A and the gymnotiform swimmer in C, the spacing of the vortex rings in the swimming direction would depend on St as indicated by Eqn 6.

membrane between fish fin rays (Lauder and Madden, 2006). The motors and other hardware were housed in a submersible cylindrical body (6.35 cm diameter) with rounded-conical caps at both ends. The total length of the robot was 60 cm.

Flow tunnel and DPIV

The robot was submerged in a variable-speed flow tunnel and supported from above on frictionless air bearings (New Way Air Bearings, Aston, PA, USA), as shown in Fig. 2A. The working section of the tunnel was 100 cm long, 33 cm wide and 32 cm deep. The air bearings permit movement along the longitudinal direction of the flow tunnel; however, the platform can also be fixed to mechanical ground through a force transducer (LSB200, Futek, Irvine, CA, USA), so that longitudinal forces can be measured, similar to the methods used in Curet et al. (Curet et al., 2011b).

A DPIV system was built to illuminate 2D planes of fluid in the water tunnel. The DPIV system was modeled after that used in Schlicke et al. (Schlicke et al., 2007). Briefly, the beam from a 2 W laser (Verdi G2, Coherent Inc., Santa Clara, CA, USA) was directed to an oscillating galvanometer mirror system (6215HM40B, Cambridge Technology Inc., Bedford, MA, USA). This oscillating mirror was located at the focal point of a custom-designed parabolic mirror, so that successive instances of the beam reflected off the parabolic mirror remained parallel, creating a strobed laser-light sheet. This light sheet was then directed into the water, illuminating silver-coated glass spheres immersed in the fluid (44 μm beads, Potter Industries, Valley Forge, PA, USA). High-speed video (FastCam 1024P PCI, Photron, San Diego, CA, USA) of the illuminated plane was recorded at the same rate that the laser beam was scanned, so that each frame recorded one transversal of the laser beam. In all experiments, the image capture rate was 500 frames s^{-1} . The width of the laser sheet was ~ 30 cm.

DPIV data were analyzed using a commercial software package (DaVis, LaVision GMBH, Göttingen, Germany). Analysis consisted of a calibration using an evenly spaced grid, video data importation and cross-correlation for velocity vector calculation. Two passes were performed for each pair of images, decreasing from an interrogation window of 64×64 pixels with 50% overlap on the first pass to 32×32 pixels with 50% overlap on the second pass. Subsequent analysis of the velocity vectors was performed in MATLAB (The MathWorks, Natick, MA, USA), as described below.

Experimental procedure

Previously, Curet et al. (Curet et al., 2011b) investigated the fixed-swimming forces and free-swimming velocities generated by the fin for a range of kinematic parameters describing an idealized traveling sinusoidal wave. The

wave used in the study prescribed the trajectories of fin ray angles relative to the vertical line, called the angular amplitude (θ), given by the following equation:

$$\theta_{\text{rays}}(x_{\text{fin}}, t) = \theta_{\text{max}} \sin \left[2\pi \left(\frac{x_{\text{fin}}}{\lambda} + ft \right) \right], \quad (7)$$

where x is the surge axis along the fin from Fig. 1C. The kinematic parameters are schematized in Fig. 1C and include maximum angular amplitude θ_{max} , frequency of ray oscillation f and wavelength λ (usually non-dimensionalized as L_{fin}/λ , which we refer to as number of undulations). For this study, a single set of kinematic parameters was chosen to be the nominal traveling wave ($\theta_{\text{max}}=30$ deg, $f=3$ Hz, number of undulations=2). All DPIV data were collected with these fin kinematic parameters.

While Curet et al. (Curet et al., 2011b) only measured free-swimming velocities in the surge direction, they noticed that the fin produces both surge and heave force components for single-traveling wave kinematics. Therefore, for a better measure of free-swimming performance, the fin must be pitched at the angle where the overall direction of thrust is aligned with the direction of flow. To estimate this angle, we performed a series of experiments over a range of pitch angles from 9 to 19 deg in which we expected to find the correct angle. For each angle, we fixed the robot to mechanical ground through a load cell to measure longitudinal force. Our setup did not allow for measurement of the vertical force. We then varied the speed of the flow around the swimming velocity expected for the nominal kinematic fin parameters while measuring force, where negative force indicated the robot swimming below its free-swimming speed and positive force indicated swimming above its free-swimming speed. The result was a linear relationship between flow speed and force with a zero crossing at the actual free-swimming speed where thrust and drag cancel. We also collected DPIV data from the midsagittal plane, which indicated the direction of the wake generated by the fin. We found that at a pitch angle of 13 deg, the swimming speed was maximized and the wake was aligned with the flow. Thus, for collection of all subsequent DPIV data, we pitched the fin at 13 deg relative to the direction of flow and set the flow speed to the measured free-swimming speed at that pitch angle. In these experiments, the deepest point of the fin was always twice the boundary layer thickness from the bottom of the tank as estimated from the DPIV data.

The DPIV planes chosen to investigate the wake generated by the fin are shown in Fig. 2B. The DPIV system is designed to allow for sagittal and horizontal planes parallel with the flow direction, and transverse planes perpendicular to the flow direction. Midsagittal plane (M) and horizontal plane (H) are composites of multiple DPIV data sets collected separately at different areas of the plane because of the limited width of the laser sheet

Table 2. Numerical simulation parameters

Parameter	FinSim	FishSim1	FishSim2	GhostbotSim
Domain size (cm ³)	72×10×24	100×18×30	60×11×12	260×40×60
Refinement ratio	4	4	4	4
No. grid levels	4	4	3	3
Grid size at coarsest level	96×10×54	144×24×24	128×24×26	196×30×45
Vorticity tagging threshold (s ⁻¹)	40	100	80	26

(original cross-correlation on the images was performed separately as well). DPIV sets from a single plane were spatially and temporally aligned. Data were linearly interpolated onto a uniform grid for display, with a vector spacing greater than the outcome of the original cross-correlation of the DPIV data. A five-frame moving average was used to temporally filter the data, an important step for the transverse planes (T1–T5) because of the noise in the data due to the fact that particles generally only stayed within the laser light sheet for a small number of frames. Lastly, the velocity vector fields were phase averaged over five full cycles ($T_{\text{cycle}}=f^{-1}=333$ ms).

Numerical simulations

In order to relate the flow structures of our robotic model back to that of the actual fish, we used fluid dynamics simulations to step from a computational model based on the body shape (MacIver and Nelson, 2000), fin shape and fin kinematics (Ruiz-Torres et al., 2013) of *A. albifrons* to a computational model of the Ghostbot fin shape and kinematics. The first simulation, FishSim1, most closely matches the kinematics measured for the 14.9 cm s⁻¹ case from Ruiz-Torres et al. (Ruiz-Torres et al., 2013). A sinusoidal traveling wave was implemented on the measured fin morphology with the time-averaged kinematic parameters reported in Ruiz-Torres et al. (Ruiz-Torres et al., 2013) (see Table 1 for details). The amplitude profile of FishSim1 was based on the maximum excursion of each ray of the actual fish kinematics. In FishSim2, the morphology, frequency and number of undulations remained the same as FishSim1, and only the amplitude profile was changed to a constant 30 deg, as indicated by the dark gray shaded entries in Table 1. RoboSim maintained the same constant amplitude profile of FishSim2, but the robot body and fin morphology were modeled. Also, the frequency and number of undulations were adjusted to match the actual robot case, indicated by the light gray shaded entries in Table 1. However, the fin wave speeds ($f\lambda$) of the RoboSim and the FishSims were similar (48 and 40 cm s⁻¹, respectively). Lastly, we also include FinSim, which simulates an undulating rectangular fin on the scale of the knife-fish fin without a body. The details of the computational method are described below.

Our computational method uses the constraint-based immersed body (cIB) method (Bhalla et al., 2013; Sharma and Patankar, 2005; Patankar et al., 2000; Patankar, 2001; Patankar and Sharma, 2005; Glowinski et al., 1999; Shirgaonkar et al., 2009; Curet et al., 2010), which is a variant of regular immersed body (IB) method of Peskin (Peskin, 2002). The cIB method solves the combined momentum equation of the fluid and immersed body (incompressible Navier–Stokes equation) while imposing the constraint of the prescribed motion of the immersed structure in a computationally efficient manner. Specifically, the combined momentum equation is solved in the computational domain \mathbf{D} represented on a Cartesian grid in the Eulerian frame of reference. The immersed body is modeled as a Lagrangian collection of immersed particles that are free to move on the background Eulerian grid. The immersed particles do not require any connectivity information and thus no explicit meshing is needed in the body domain, as is generally needed in the finite element type (FEM) methods. The presence of the immersed body is modeled via an additional body force in the incompressible Navier–Stokes equation that is present only inside the volume region physically occupied by the immersed body at any given time-instant. The IB method and its variants, such as the cIB method, permit the usage of fast Cartesian grid solvers, which are otherwise difficult to use with the unstructured grids employed within the FEM framework.

To further reduce the computational cost of resolving fine flow features near the body of the fish and the robot, we solve the incompressible Navier–Stokes equation on a block-structured locally refined Cartesian grid

as detailed by Griffith and others (Griffith, 2009; Griffith, 2012; Griffith and Peskin, 2005; Griffith, 2005; Griffith et al., 2007). The locally refined Cartesian grid consists of hierarchy of grid levels, which are denoted by $l=0, 1, \dots, l_{\text{max}}$. Level $l=0$ denotes the coarsest level in the grid hierarchy and $l_{\text{max}} \geq 0$ denotes the finest level. Each level of the hierarchical grid is composed of one or more rectangular Cartesian grid patches on which the combined momentum equation is discretized. We denote the Cartesian grid spacing on level l of the locally refined grid by h^l . This grid spacing is related to the grid spacing on the next coarser level $l-1$ by an integer refinement ratio n_{ref}^{l-1} , so that:

$$h^l = \frac{1}{n_{\text{ref}}^{l-1}} h^{l-1}. \quad (8)$$

The immersed structure is placed on the finest grid level so that the thin boundary layers are accurately resolved. We also tag regions of \mathbf{D} where the magnitude of the vorticity vector, $|\boldsymbol{\omega}|$, reaches a certain threshold value. This helps us to deploy fine grid structures to accurately capture the vortex structures shed from the immersed interfaces without requiring finer resolution in other parts of \mathbf{D} . The details of the numerical method and its validation for various benchmark problems can be found in Bhalla et al. (Bhalla et al., 2013).

The outlined numerical scheme is implemented in IBAMR (IBAMR, 2013), an open-source C++ library that provides support for fluid–structure interaction models that are based on the IB method. IBAMR uses SAMRAI (SAMRAI, 2007; Hornung and Kohn, 2002; Hornung et al., 2006), PETSc (Balay et al., 2009; Balay et al., 2008; Balay et al., 1997), *hypre* (HYPRE, 2011; Falgout and Yang, 2002) and libMesh (libMesh, 2013; Kirk et al., 2006) libraries, among others, for its functionality.

The simulations were carried out in a 3D rectangular computational domain \mathbf{D} . In all simulations, zero-velocity boundary conditions were imposed on the domain boundaries, except for the simulations performed for the FinSim case. For the FinSim case, periodic boundary conditions were imposed on the domain in the rostrocaudal direction, and zero-velocity boundary conditions were used for the remaining boundaries. Details of the domain size, refinement ratio, number of grid levels and coarsest grid size, and vorticity threshold used for tagging high-gradient vortex regions are reported in Table 2.

Computing environment

The numerical simulations were carried at the Northwestern University Quest supercomputing facility. The cluster is made up of 502 nodes, each consisting of eight 64 bit, 2.26 GHz Intel Nehalem E5520 processors with 48 Gb of memory for each node.

Acknowledgements

We thank George Lauder for his helpful discussions concerning fish swimming mechanics and DPIV analysis. We also thank James Snyder for his help in programming the Ghostbot as well as Stuart Cameron for his advice on the design of the DPIV system.

Competing interests

The authors declare no competing financial interests.

Author contributions

M.A.M. led the experimental fluids and robotics efforts. I.D.N. and O.M.C. developed the robotic experiments. I.D.N. ran and analyzed the DPIV experiments. N.A.P. led the computational fluid analysis effort. A.P.S.B. wrote the computational fluid dynamics code. R.B. ran the simulations and visualized and analyzed simulation data. I.D.N. wrote the manuscript with contributions from A.P.S.B., R.B., O.M.C. and M.A.M.

Funding

This work was supported by National Science Foundation (NSF) grants IOB-0517683 and DGE-0903637 to M.A.M. and by an NSF grant CMMI-0941674 to M.A.M. and N.A.P. Partial support was provided by NSF grants CBET-1066575 to N.A.P. and CBET-0828749 to N.A.P. and M.A.M. O.M.C acknowledges the support of a Diversifying Higher Education Faculty in Illinois Program fellowship. Computational resources were provided by Northwestern University High Performance Computing System – Quest.

Supplementary material

Supplementary material available online at <http://jeb.biologists.org/lookup/suppl/doi:10.1242/jeb.091520/-/DC1>

References

- Anderson, J., Streitlien, K., Barrett, D. and Triantafyllou, M. (1998). Oscillating foils of high propulsive efficiency. *J. Fluid Mech.* **360**, 41–72.
- Balay, S., Eijkhout, V., Gropp, W. D., McInnes, L. C. and Smith, B. F. (1997). Efficient management of parallelism in object oriented numerical software libraries. In *Modern Software Tools in Scientific Computing* (ed. E. Arge, A. M. Bruaset and H. P. Langtangen), pp. 163–202. Boston, MA: Birkhäuser Press.
- Balay, S., Buschelman, K., Eijkhout, V., Gropp, W. D., Kaushik, D., Knepley, M. G., McInnes, L. C., Smith, B. F. and Zhang, H. (2008). PETSc users manual. Technical Report ANL-95/11, revision 3.0.0. Lemont, IL: Argonne National Laboratory.
- Balay, S., Buschelman, K., Gropp, W. D., Kaushik, D., Knepley, M. G., McInnes, L. C., Smith, B. F. and Zhang, H. (2009). PETSc. Portable, extensible toolkit for scientific computation. Available at <http://www.mcs.anl.gov/petsc>.
- Bhalla, A. P. S., Bale, R., Griffith, B. E. and Patankar, N. A. (2013). A unified mathematical framework and an adaptive numerical method for fluid-structure interaction with rigid, deforming, and elastic bodies. *J. Comput. Phys.* **250**, 446–476.
- Blake, R. W. (1983). Swimming in the electric eels and knife-fishes. *Can. J. Zool.* **61**, 1432–1441.
- Blondeaux, P., Fornarelli, F., Guglielmini, L., Triantafyllou, M. S. and Verzicco, R. (2005). Numerical experiments on flapping foils mimicking fish-like locomotion. *Phys. Fluids* **17**, 113601.
- Borazjani, I. and Sotiropoulos, F. (2008). Numerical investigation of the hydrodynamics of carangiform swimming in the transitional and inertial flow regimes. *J. Exp. Biol.* **211**, 1541–1558.
- Borazjani, I. and Sotiropoulos, F. (2009). Numerical investigation of the hydrodynamics of anguilliform swimming in the transitional and inertial flow regimes. *J. Exp. Biol.* **212**, 576–592.
- Cowan, N. J. and Fortune, E. S. (2007). The critical role of locomotion mechanics in decoding sensory systems. *J. Neurosci.* **27**, 1123–1128.
- Curet, O. M., AlAli, I. K., MacIver, M. A. and Patankar, N. A. (2010). A versatile implicit iterative approach for fully resolved simulation of self-propulsion. *Comput. Methods Appl. Mech. Eng.* **199**, 2417–2424.
- Curet, O. M., Patankar, N. A., Lauder, G. V. and MacIver, M. A. (2011a). Aquatic manoeuvring with counter-propagating waves: a novel locomotive strategy. *J. R. Soc. Interface* **8**, 1041–1050.
- Curet, O. M., Patankar, N. A., Lauder, G. V. and MacIver, M. A. (2011b). Mechanical properties of a bio-inspired robotic knife-fish with an undulatory propulsor. *Bioinspir. Biomim.* **6**, 026004.
- Dewey, P. A., Carriou, A. and Smits, A. J. (2012). On the relationship between efficiency and wake structure of a batoid-inspired oscillating fin. *J. Fluid Mech.* **691**, 245–266.
- Dubief, Y. and Delcayre, F. (2000). On coherent-vortex identification in turbulence. *J. Turbulence* **1**, 11.
- Falgout, R. D. and Yang, U. M. (2002). *hypre*: a library of high performance preconditioners. In *Computational Science – ICCS 2002 Part III (Lecture Notes in Computer Science, Vol. 2331)* (ed. P. M. A. Sloot, C. J. K. Tan, J. J. Dongarra and A. G. Hoekstra), pp. 632–641. Berlin: Springer-Verlag.
- Glowninski, R., Pan, T.-W., Hesla, T. I. and Joseph, D. D. (1999). A distributed Lagrange multiplier/fictitious domain method for particulate flows. *Int. J. Multiphase Flow* **25**, 755–794.
- Griffith, B. E. (2005). *Simulating the Blood-Muscle-Valve Mechanics of the Heart by an Adaptive and Parallel Version of the Immersed Boundary Method*. PhD thesis, Courant Institute of Mathematical Sciences, New York University, New York, NY.
- Griffith, B. E. (2009). An accurate and efficient method for the incompressible Navier-Stokes equations using the projection method as a preconditioner. *J. Comput. Phys.* **228**, 7565–7595.
- Griffith, B. E. (2012). Immersed boundary model of aortic heart valve dynamics with physiological driving and loading conditions. *Int. J. Numer. Meth. Biomed. Engng.* **28**, 317–345.
- Griffith, B. E. and Peskin, C. S. (2005). On the order of accuracy of the immersed boundary method: higher order convergence rates for sufficiently smooth problems. *J. Comput. Phys.* **208**, 75–105.
- Griffith, B. E., Hornung, R. D., McQueen, D. M. and Peskin, C. S. (2007). An adaptive, formally second order accurate version of the immersed boundary method. *J. Comput. Phys.* **223**, 10–49.
- Hornung, R. D. and Kohn, S. R. (2002). Managing application complexity in the SAMRAI object-oriented framework. *Concurrency Computat. Pract. Exper.* **14**, 347–368.
- Hornung, R. D., Wissink, A. M. and Kohn, S. R. (2006). Managing complex data and geometry in parallel structured AMR applications. *Eng. Comput.* **22**, 181–195.
- HYPRE (2011). *hypre*: high performance preconditioners. Livermore, CA: Lawrence Livermore National Laboratory. Available at <https://www.llnl.gov/CASC/hypre>.
- IBAMR (2013). IBAMR: an adaptive and distributed-memory parallel implementation of the immersed boundary method. Available at <https://code.google.com/p/ibamr/>.
- Kern, S. and Koumoutsakos, P. (2006). Simulations of optimized anguilliform swimming. *J. Exp. Biol.* **209**, 4841–4857.
- Kirk, B., Peterson, J. W., Stogner, R. H. and Carey, G. F. (2006). libMesh: a C++ library for parallel adaptive mesh refinement/coarsening simulations. *Eng. Comput.* **22**, 237–254.
- Krahe, R. and Fortune, E. S. (2013). Electric fishes: neural systems, behaviour and evolution. *J. Exp. Biol.* **216**, 2363–2364.
- Kuethe, J. and Schetzler, A. (1950). *Foundations of Aerodynamics*, Section 2.14. New York, NY: Wiley.
- Lauder, G. V. and Madden, P. G. A. (2006). Learning from fish: kinematics and experimental hydrodynamics for roboticists. *Int. J. Autom. Comput.* **3**, 325–335.
- Lauder, G. V. and Tytell, E. D. (2006). Hydrodynamics of undulatory propulsion. In *Fish Biomechanics* (ed. R. E. Shadwick and G. V. Lauder), pp. 425–468. New York, NY: Praeger.
- libMesh (2013). libMesh: C++ finite element library. Available at <http://libmesh.sourceforge.net>.
- Lighthill, J. and Blake, R. (1990). Biofluidynamics of balistiform and gymnotiform locomotion. Part 1. Biological background, and analysis by elongated-body theory. *J. Fluid Mech.* **212**, 183–207.
- MacIver, M. A. and Nelson, M. E. (2000). Body modeling and model-based tracking for neuroethology. *J. Neurosci. Methods* **95**, 133–143.
- MacIver, M. A., Sharabash, N. M. and Nelson, M. E. (2001). Prey-capture behavior in gymnotid electric fish: motion analysis and effects of water conductivity. *J. Exp. Biol.* **204**, 543–557.
- MacIver, M. A., Patankar, N. A. and Shirgaonkar, A. A. (2010). Energy-information trade-offs between movement and sensing. *PLOS Comput. Biol.* **6**, e1000769.
- Moored, K., Dewey, P., Smits, A. and Haj-Hariri, H. (2012). Hydrodynamic wake resonance as an underlying principle of efficient unsteady propulsion. *J. Fluid Mech.* **708**, 329.
- Nauen, J. C. and Lauder, G. V. (2002). Hydrodynamics of caudal fin locomotion by chub mackerel, *Scomber japonicus* (Scombridae). *J. Exp. Biol.* **205**, 1709–1724.
- Neveln, I. D., Bai, Y., Snyder, J. B., Solberg, J. R., Curet, O. M., Lynch, K. M. and MacIver, M. A. (2013). Biomimetic and bio-inspired robotics in electric fish research. *J. Exp. Biol.* **216**, 2501–2514.
- Patankar, N. A. (2001). A formulation for fast computations of rigid particulate flows. In *Annual Research Briefs*, pp. 185–196. Stanford, CA: Center for Turbulence Research.
- Patankar, N. A. and Sharma, N. (2005). A fast projection scheme for the direct numerical simulation of rigid particulate flows. *Commun. Numer. Methods Eng.* **21**, 419–432.
- Patankar, N. A., Singh, P., Joseph, D., Glowinski, R. and Pan, T. (2000). A new formulation of the distributed Lagrange multiplier/fictitious domain method for particulate flows. *Int. J. Multiphase Flow* **26**, 1509–1524.
- Peskin, C. (2002). The immersed boundary method. *Acta Numerica* **11**, 479–517.
- Ruiz-Torres, R., Curet, O. M., Lauder, G. V. and MacIver, M. A. (2013). Kinematics of the ribbon fin in hovering and swimming of the electric ghost knife-fish. *J. Exp. Biol.* **216**, 823–834.
- SAMRAI (2007). *SAMRAI: Structured Adaptive Mesh Refinement Application Infrastructure*. Livermore, CA: Lawrence Livermore National Laboratory. Available at <https://www.llnl.gov/CASC/SAMRAI>.
- Schlicke, T., Cameron, S. and Coleman, S. (2007). Galvanometer-based PIV for liquid flows. *Flow Meas. Instrum.* **18**, 27–36.
- Sefati, S., Neveln, I., Roth, E., Mitchell, T., Snyder, J. B., MacIver, M. A., Fortune, E. S. and Cowan, N. J. (2013). Mutually opposing forces during locomotion can eliminate the tradeoff between maneuverability and stability. *Proc. Natl. Acad. Sci.* **110**, 18798–18803.
- Sfakiotakis, M., Lane, D. M. and Davies, J. B. C. (1999). Review of fish swimming modes for aquatic locomotion. *IEEE J. Ocean. Eng.* **24**, 237–252.
- Sharma, N. and Patankar, N. A. (2005). A fast computation technique for the direct numerical simulation of rigid particulate flows. *J. Comput. Phys.* **205**, 439–457.
- Shirgaonkar, A. A., Curet, O. M., Patankar, N. A. and MacIver, M. A. (2008). The hydrodynamics of ribbon-fin propulsion during impulsive motion. *J. Exp. Biol.* **211**, 3490–3503.
- Shirgaonkar, A. A., MacIver, M. A. and Patankar, N. A. (2009). A new mathematical formulation and fast algorithm for fully resolved simulation of self-propulsion. *J. Comput. Phys.* **228**, 2366–2390.
- Snyder, J. B., Nelson, M. E., Burdick, J. W. and MacIver, M. A. (2007). Omnidirectional sensory and motor volumes in electric fish. *PLoS Biol.* **5**, e301.
- Taylor, G. K., Nudds, R. L. and Thomas, A. L. (2003). Flying and swimming animals cruise at a Strouhal number tuned for high power efficiency. *Nature* **425**, 707–711.
- Triantafyllou, M., Triantafyllou, G. and Gopalkrishnan, R. (1991). Wake mechanics for thrust generation in oscillating foils. *Phys. Fluids A* **3**, 2835–2837.
- Turner, R. W., Maler, L. and Burrows, M. (1999). Special issue on electroreception and electrocommunication. *J. Exp. Biol.* **202**, 1167–1458.
- Tytell, E. D. and Lauder, G. V. (2004). The hydrodynamics of eel swimming. I. Wake structure. *J. Exp. Biol.* **207**, 1825–1841.
- Tytell, E. D., Borazjani, I., Sotiropoulos, F., Baker, T. V., Anderson, E. J. and Lauder, G. V. (2010). Disentangling the functional roles of morphology and motion in the swimming of fish. *Integr. Comp. Biol.* **50**, 1140–1154.